Electronic Circuits and Architectures
Mekelweg 4,
2628 CD Delft
The Netherlands
https://elca.tudelft.nl/

M.Sc. Thesis

Assessment of EMF exposure in 5G FR2 band in practical indoor scenarios with beamforming transmitter

Junhan Gui

Abstract

Not only did the fifth generation mobile communication system increase the data rate, capacity and coverage, but also raise a public concern regarding human exposure to electromagnetic fields (EMFs). This thesis project assessed EMF exposure in practical indoor scenarios with a beamforming transmitter through electromagnetic and biologic level of simulations and a validation framework. 3D indoor environments were constructed based on measured dielectric constants of materials, enabling realistic ray-tracing simulations in beamforming scenarios. The obtained simulation results were then combined to a multi-layer skin model to evaluate localized absorption mechanisms. This study also highlighted the influence of environmental geometry on exposure levels. An algorithm of bridging the gap between indoor wave propagation and exposure assessment regarding biological tissues was proposed for the first time. It is illustrated by the results that beamforming technology introduced time and user dependency to the exposure levels, while these predicted values remained well below the limit in ICNIRP of 20 W/m^2.

Assessment of EMF exposure in 5G FR2 band in practical indoor scenarios with beamforming transmitter

---

Thesis

submitted in partial fulfillment of the
requirements for the degree of

Master of Science

in

Electrical Engineering

by

Junhan Gui
born in Chengdu, China

This work was performed in:

Electronic Circuits and Architectures Group
Department of Microelectronics
Faculty of Electrical Engineering, Mathematics and Computer Science
Delft University of Technology

Delft University of Technology

Delft University of Technology
Department of
Microelectronics

The undersigned hereby certify that they have read and recommend to the Faculty of Electrical Engineering, Mathematics and Computer Science for acceptance a thesis entitled **"Assessment of EMF exposure in 5G FR2 band in practical indoor scenarios with beamforming transmitter"** by **Junhan Gui** in partial fulfillment of the requirements for the degree of **Master of Science**.

Dated: 27.08.2025

Chairman: _____
dr. M. Spirito

Advisor: _____
dr. Y. Aslan

Committee Members: _____
dr. M. Mastrangeli

_____

Abstract

Not only did the fifth generation mobile communication system increase the data rate, capacity and coverage, but also raise a public concern regarding human exposure to electromagnetic fields (EMFs). This thesis project assessed EMF exposure in practical indoor scenarios with a beamforming transmitter through electromagnetic and biologic level of simulations and a validation framework. 3D indoor environments were constructed based on measured dielectric constants of materials, enabling realistic ray-tracing simulations in beamforming scenarios. The obtained simulation results were then combined to a multi-layer skin model to evaluate localized absorption mechanisms. This study also highlighted the influence of environmental geometry on exposure levels. An algorithm of bridging the gap between indoor wave propagation and exposure assessment regarding biological tissues was proposed for the first time. It is illustrated by the results that beamforming technology introduced time and user dependency to the exposure levels, while these predicted values remained well below the limit in ICNIRP of 20 W/m^2.

Acknowledgments

I would like to thank my advisors Marco Spirito and Yanki Aslan for their assistance during the writing of this thesis, my daily supervisor Leila Gottmer for her patience and support, and dr. J Bueno Lopez, ir. P.J. Aubry, Gaetano Chirico, Máté Iványi, Ehsan Shokrolahzade for their help in the measurement. Gratitude goes to all the fellow students as well. Without them, this would not have been possible.

Junhan Gui
Delft, The Netherlands
27.08.2025

Contents

List of Figures

List of Tables

1 Introduction

In this chapter, an overview of the thesis work is given. To be specific, section 1.1 explains basic concepts of the topic and motivation of research. Significance of it is also included. The formulation of the research problem is presented in section 1.2. After that, a brief summary regarding relevant works is presented in section 1.3, at the end of which gaps of previous works are identified. Additionally, approaches proposed by this work to address the gaps are mentioned. Following that, thesis scopes and novelties are listed in section 1.4 and 1.5. Finally, section 1.6 states how the following parts of the thesis are organized.

1.1 Motivation

EMF is defined as a region of space where electric and magnetic forces are produced upon charged particles within it [1]. The oscillation rate of such a field is called frequency and radio frequency (RF) EMF refers to such a field in the range of 3 kHz to 300 GHz.

Despite many uses of it, there are also evidences that RF EMF is harmful to human health under certain circumstances. For example, specific asymmetric EMF can reduce the healing speed of broken bones [2]. In addition, indirect damage can be caused by unintentional interference with RF tools used as medical treatment [3].

It is clear that with an increasing exposure level, the extend of the potential damages enlarges. Therefore, with the advance in wireless communication, 5G technology not only provided a higher traffic data, but also raises the concern in EMF exposure towards users [4, 5].

With various possible consequences caused by EMF exposure, regulations have been developed to set a limit on personal exposure. According to [3], different regulations are applied to different frequency ranges. When the frequency is above 6 GHz, EMF is absorbed more superficially, leading to a change of the indicator of exposure level from absorbed power over mass to absorbed power over area.

To sum up, the emerging technologies has lead to an increasing concern regarding exposure and human health. Meanwhile, there is also a lack of suitable method to evaluate the new indicator. Therefore, accurate techniques for EMF exposure assessment given the operating frequency range of current and future wireless communication net-

works are required. As a result, this thesis project aims at developing a simulation-level algorithm of indoor EMF exposure assessment.

1.2 Problem formulation

With the advantages of high data rate, low latency and the reliability in crowded environment, the implementation of 5G has seen a growth. However, along comes the heath concern with on EMF exposure [4].

Figure 1.1: 5G applications at the city level

As shown in Fig. 1.1, multiple devices has been installed in a modern city. Yet there is still a lack of study regarding assessment in 5G FR2. Therefore, this work is motivated to combine the electromagnetic level of EMF exposure assessment in 5G FR2 to a biological skin model.

Although a considerable amount of work has been done concerning RF-EMF exposure assessment below 6 GHz [6]. However, features of 5G have made the previous methods unsuitable. The main challenges regarding EMF exposure assessment in 5G FR2 are listed below.

Firstly, to increase spectral efficiency, beamforming technology is applied, which enables the generation of time dependent radiation patterns towards active users [4, 7].

This leads to a time variant exposure level regarding the downlink (DL) requirement of user equipments (UEs). Thus, propagation scenarios need to be specified to create realistic predictions of EMF exposure levels.

Moreover, the increased operating frequency increases from previous generations leads to a requirement of specification of the surrounding environment. [4]. To be specific, 5G FR2 starts from 24.25 GHz [4].

According to [5, 8], at a higher frequency, the wave is more attenuated by the same indoor environment. When it comes to indoor scenarios such as a meeting room, the consideration of geometrical layout of the room becomes necessary. In addition to materials used in the environment, the reactions of human skin also differ at various frequencies, making it harder to accurately map the propagation environment [9].

In addition to analysis of scattering features in practical features, the assessment of exposure that goes to specific skin structures is significant, too. Such details of skin tissues were not considered in below 6 GHz framework, as the thickness of skin is relatively small compared to the wavelength [6]. Similarly, the chanllenges lie in defining a realistic model of the skin. Afterwards, a practical level of transmitted power is required.

Thus, to solve the challenges mentioned above and fill the gap between previous EMF exposure assessment methods and implementation of 5G technologies, the research problem of this thesis project is defined as development of a complete workflow of EMF exposure assessment that merges propagation simulations at indoor and skin levels.

1.3 Literature review

As mentioned above, the attenuation of millimeter wave (mmWave) in indoor environments is significantly influenced by the geometric layout [5, 8, 10]. Therefore, to realistically assess the power levels at the surface of a user, it is crucial to simulate and measure the mmWave behavior.

This can be divided into multiple aspects, namely operating frequency, layout and material property of the environment, and the distribution and density of users.

Firstly, the same indoor environment is considered to quantify the effect of frequency. J. Li et el. conducted channel measurements at various frequencies from 2 GHz to 26 GHz [11, 12]. In [11], both a uniform linear and a uniform planar array (UPA) of 64 elements were applied. Meanwhile, a 8×16-elements planar was also implemented. This showed the influence of the operating frequency on wave propagation in the same indoor environment. Such measurements helped calibrate a ray-tracing simulator with a 1024-element planar array. Similar measurement of indoor and outdoor environments at 28 GHz were conducted in [13] and [14] respectively.

Secondly, the dielectric properties of materials are crucial factors as well. Work of S.Deng, M.K.Samimi and T.S.Rappaport presented a more detailed indoor model of a typical office environment where walls and doors of different materials were im-

plemented [8]. Additionally, both directional and omnidirectional loss models were considered. Relatively more realistic path loss exponents were obtained and the results also showed that with the increase of frequency, both path loss increased [8].

Finally, the distribution and density of users are taken into consideration. For a higher user density environments such as meeting room, library and event halls, different user scenarios were considered in [5]. A two-floor library building was selected as the indoor environment. Material properties at the simulation frequency were taken into consideration with the human skin dielectric property computed from [15]. Not only did the number of user make an influence on the DL requirement, it also modified the environmental features. Therefore, two cases of full capacity with 202 users and 70% capacity with 140 users were testified separately. The results showed that within the same indoor environment, a higher user density led to a higher exposure level, while under all conditions the safety limits were met. Meanwhile, it also showed that the attenuation increased at a higher operating frequency.

In addition to proper definitions of indoor environment and antenna radiation pattern, further simulations are needed regarding assessment of exposure levels.

A series of simulations conducted by M. Bonato et al. considered single-user indoor scenarios [16, 17, 18]. [16, 17] focused on the exposure levels at 3.7 GHz. According to [3], for frequency range under 6 GHz, the indicator of exposure is expressed by the absorbed power in a piece of tissue weighed 10 grams. While for 5G FR2, the absorption rate is averaged over a 4 mm^2 surface for 6 minutes [3].

In [18], a simulation at 14 GHz was also conducted, in which range the standard remains the same. For the simulations at 3.7 GHz, a full human body model of a child was applied while due to simulation cost, only half of the adult body model was considered. Meanwhile, three positions of the UPA were applied. When it came to the 1024-element array, it was placed 50 cm laterally to the head of models as where the strongest exposure level was obtained in the lower frequency simulations. Additionally, only head areas were considered in these cases.

The Sim4Life platform made it possible to perform full-wave simulations with geometric and electromagnetic characteristics of human heads considered[18]. However, given the penetration depth of human skin at 5G FR2, this could be a waste of computational source. To avoid that, there is an increasing interest in the EMF behavior in skin tissues only.

For example, in [19], energy absorption of a homogeneous human skin model given various antennas at 2 GHz and 24 GHz was studied. This work proved the necessity of advancing the simulation to the skin level. To this extend, the structures of skin is simplified, similar to the materials used to construct the indoor environment. However, due to the layered feature of the skin, a multi-layer model with known dielectric properties is more representative [20]. Similar experiment was conducted in the frequency range of 20 - 28 GHz by N. M. Tamyis et al. [21].

Meanwhile, as blood is the only tissue that flows throughout your body, biological studies are focused on the exposure going to blood vessels [22]. However, experiments were conducted by emitting EMF directly to extracted red blood cells (RBCs). This introduced a gap between the practical received power levels at the blood vessel and the transmitted power in biological experiments.

To conclude, there are mainly gaps to address in previous works.

To conclude, studies in areas of dielectric properties of environmental materials and human skin, wave propagation simulation, and exposure assessment have been conducted, respectively, however, also individually regarding 5G FR2. As a result, there are still gaps between each step such that an overall workflow of indoor EMF exposure assessment in 5G FR2 with beamforming cannot be formed.

1.4 Thesis scope and objectives

The thesis scope is to develop a tool for exposure assessment in practical indoor scenarios with beamforming transmitter in 5G FR2 and demonstrate with an indoor propagation measurement. To narrow the case down to several realistic scenarios, the scopes of the project are defined with the following limitations and assumptions.

- Indoor environment based on a room layout in TU Delft EEMCS with empirical values as dielectric properties of the materials of construction. Tables and chairs simulated by floating boards as only furniture inside.

- 26.5 GHz band operation.

- A 4×4 active array called BBox as transmitter, a lens-based 5G mmWave EMF sensor as receiver.

- Cell partition and beam switching to cell centers.

- Isotropic receivers for the ray tracing simulations.

- A multi-layer skin model based on biological properties.

1.5 Thesis novelty

To combine different levels of simulations and perform realistic prediction of EMF exposure levels, efforts are taken migrating indoor 3D ray tracing results to EMF mechanisms in human skin layers in this work. The novel aspects are listed below:

- A new propagation environment setup with empirical complex permittivity of

materials measured by an open-ended coaxial probe is created. Practical and reliable ray tracing results are generated and discrepancies are identified and motivated.

- First time merged an indoor propagation simulation with an EMF exposure assessment at skin level. Addressed the gap between simulations of indoor mmWave propagation and biologic tissues.

- Proposed an approach to testifying indoor beamforming algorithms by measuring EMF with a 5G beamforming antenna array.

1.6 Thesis outline

The rest of the thesis is organized as follows. Chapter 2 provides detailed information about simulation and validation of the indoor propagation part. Chapter 3 showed how the propagation results are applied to a multi-layer skin model. Overall and structural exposures are assessed. Conclusion and suggestion of the future work is presented in Chapter 4.

2 Indoor propagation

This chapter targets at illustrating the methodology of the indoor propagation simulation and an additional measurement.

Starting with 2.1, a 3D database was constructed based on the measured dimensions and dielectric properties of the materials. 2.2 demonstrates the preparation steps of the ray tracing simulation, namely a creation of an antenna radiation pattern and a beamforming algorithm. The ray tracing results were then displayed and analyzed in 2.4. Eventually, 2.5 described the measurement that was carried out to validate the simulations.

2.1 Simulation environment description

This section shows how a practical room, called Snijderszaal, in the EWI building of TU Delft is measured and mapped to a 3D model for the wave propagation simulation.

The chosen indoor scenario is a rectangular-shaped meeting room with a single entrance located on the inner wall, which connects to the corridor. The other three sides consist of glass windows, concrete supports, and radiators mounted against them. Pillars are aligned with the walls and continue to the ceiling.

In addition to the built-in features, there is also movable furniture inside the room. For example, tables and chairs can be rearranged to meet the requirements of different purposes. In this project, two scenarios are considered, namely a presentation scenario and a meeting scenario.

As shown in Fig. 2.1a, in the presentation scenarios, tables are put away and chairs are arranged in a 6×6 grid. By comparison, in the meeting scenario in Fig. 2.1b, tables are formed to a circular layout with space left in the center.

In the WallMan interface, a solid can be created by defining the material and dimensions of it. With the combination of structures, a 3D model can be constructed to represent the indoor propagation environment, in which ray tracing simulations are conducted afterwards. The phrase indoor database, or the word database is used to describe such a model of the propagation environment in the following context. The database of the Snijderszaal with no furniture nor users inside was numbered as database 1.

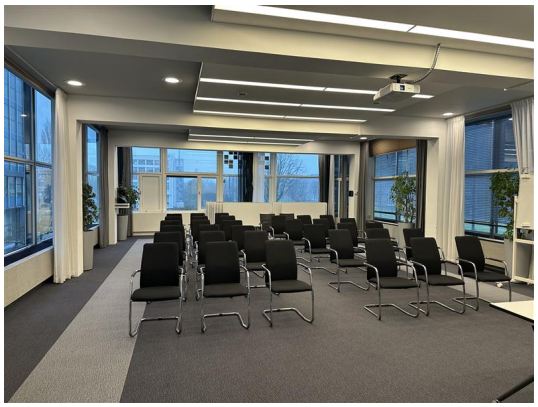

(a) View of the presentation scenario

(b) View of the meeting scenario

Figure 2.1: Selected indoor environment of wave propagation analysis

With a laser distance meter, the dimensions of the Snijderszaal were measured. The model was simplified with the following structures considered:

- The wall of the entrance side, pillars go up to the ceiling and turned horizontal below it, the ceiling were considered using the same material. This is marked as material 1.

- The 3 other side walls consist of windows and radiators. The material of them are numbered as material 2 and material 3.

- A few boards connected to the lower surface of the pillar, marked as material 4.

- The ground of the room was represented by the material of the carpet covering it. The material index of it is 5.

- The top surfaces of chairs and tables, knowing as material 6 and 7 respectively.

However, due to the lack of knowledge of materials used for these structures, an open-ended coaxial probe was used to measure the dielectric constants to make the database electromagnetically accurate.

$$\varepsilon_r^*(\omega) = \varepsilon_r'(\omega) - j\varepsilon_r''(\omega) = \varepsilon_r'(\omega) - j\frac{\sigma(\omega)}{\omega\varepsilon_0} \tag{2.1}$$

As shown in Eq. (2.1), relative permittivity can be expressed by permittivity and conductivity [23]. In such a formula, ω represents the angular frequency, and ϵ_r' and ϵ_r'' are the real and imaginary parts of the relative complex permittivity respectively. ϵ_0 is the permittivity of the vacuum. Meanwhile, σ stands for conductivity.

The measurement began with a calibration as shown in Fig. 2.2a. As one of the liquids whose dielectric properties are well known, methanol is chosen as the calibration

material [24, 25]. The calibration and one of the measurement setups are displayed in Fig. 2.2.

(a) Calibration setup

(b) Measurement setup

Figure 2.2: Calibration and measurement setup with an open-ended coaxial probe

As shown in Eq. (2.2), when the frequency increases, the skin depth decreases accordingly. Therefore, at 26.5 GHz, the skin depths of materials are fairly small. The specific values at 26.5 GHz were computed and listed in the table below, with non-magnetic assumption. As a result, the thickness is considered less influential given it is much larger than the skin depth. The same holds for multilayer structures such as the radiator. It is assumed that the outer layer contributes the most.

$$\delta = 1/\sqrt{\pi f \mu \sigma} \tag{2.2}$$

As a result, the model was simplified by using the dielectric properties of materials of the exposed surfaces only. Eventually, seven materials were measured for the construction of the 3D database. Regarding each of them, five measurements were conducted and the average values at 26.5 GHz were calculated and shown in the table below. σ' represents the real part of the conductivity.

Material	ϵ_r'	ϵ_r''	$\sigma'[S/m]$	$\delta[mm]$
1	1.45	0.368	0.543	4.196
2	2.20	0.777	1.145	2.889
3	3.10	0.418	0.616	3.939
4	1.85	0.446	0.658	3.811
5	1.07	0.194	0.286	5.781
6	1.15	0.077	0.114	9.157
7	3.53	0.317	0.46	4.559

Table 2.1: Measured material properties at 26.5 GHz

In addition to Table. 2.2, the relative complex permittivity and electric conductivity of human skin at body temperature was obtained from [9]. With such values, the

scattering of users can then be taken into account.

Material	ϵ_r'	ϵ_r''	σ
Skin-Epidermis + dermis	17.48109	13.08136	19.28493

Table 2.2: Skin electromagnetic properties at 26.5 GHz

Once the dielectric constants of the materials needed to model the room were measured, 3D databases can be constructed in the WallMan interface.

As shown in Fig. 2.3, a simplified indoor model with no furniture inside was created. The database of this layout is called database empty.

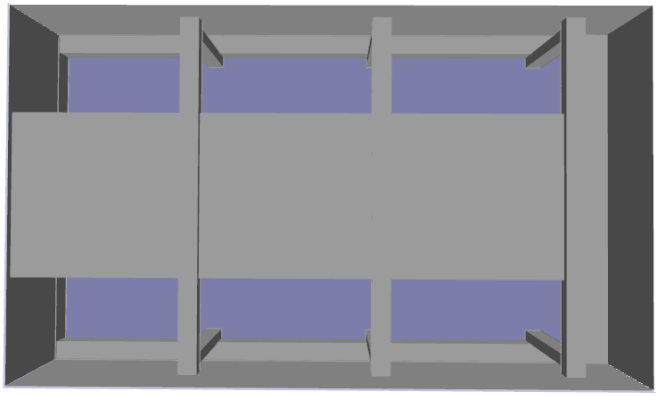

Figure 2.3: 3D database of the Snijderszaal without furniture

Efforts were taken to quantify the influence of scattering factors, namely tables, chairs and the users. Given the using scenarios of the Snijderszaal, the target is to maximize the user density at the simulation level. To accomplish that, the beamforming scenarios are required to be defined.

2.2 Excitation pattern and grid of beams

In this section, development process of the excitation source and the beamforming algorithm is illustrated. Details of the UPA simulation are shown in 2.2.1. The general simulation setups were mentioned in 2.2.2, based on which simulation aiming at dividing the room into grids was conducted. After that, the final division was shown in 2.2.3.

2.2.1 Antenna modeling

A microstrip patch antenna (MPA) consists of three basic layers, namely the ground plane, the substrate, and the patch [26]. The fact that both the active and the passive circuit can be etched on the same substrate makes it easy to fabricate. It also offers advantages such as low profile and compactness.

A 5G beamforming antenna called BBox is implemented in the final measurement in the indoor environment. The structure of such an antenna is shown in Fig. 2.4, It is a UPA with 4 × 4 series MPA.

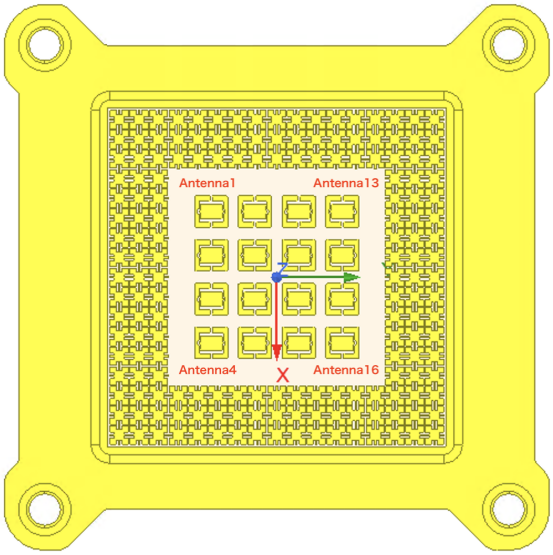

Figure 2.4: BBox antenna image

Therefore, to create a representative radiation pattern for propagation simulation, a UPA with 4 × 4 half-wavelength coaxial feed MPAs with half-wavelength spacing at 26.5 GHz was simulated in CADFEKO. The design parameters of a single MPA are shown below.

Design parameters	Values	Units
Substrate & outer coaxial pin ϵ'	2.2	
Patch (w × l)	3.35 × 3.35	mm
Substrate (w × l × h)	5.66 × 5.66 × 0.5	mm
Outer coaxial pin radius	0.69	mm
Inner coaxial pin radius	0.2	mm
Pin offset	1	mm
Coaxial pin length	0.7	mm

Table 2.3: Single patch antenna parameters

Perfect electrical conductor (PEC) was used as the material for both the patch and

the ground plane. With the same dimensions as the substrate, the ground plane was simulated by changing the bottom surface of the substrate cuboid into PEC. Meanwhile, the length of the coaxial feed would not affect the radiation pattern. Therefore, to reduce the meshing complexity and the simulation time, it was defined as 0.2 mm longer than the substrate height.

Once a single element was defined, the UPA was constructed by replication. Waveguide ports with normalized magnitude and zero phases were then attached to the feed pins. 3D far field results were required.

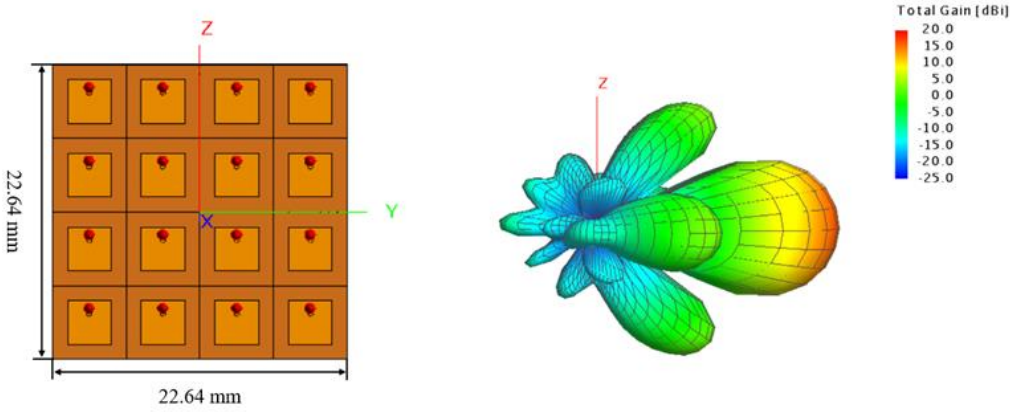

Figure 2.5: UPA (16 elements) at 26.5 GHz

The operating frequency of the BBox is from 26.5 to 29.5 GHz [27]. At the central frequency of 28 GHz, the typical transmitter EIRP is 41.5 dBm. The simulated pattern reached a directivity of 16.7 dBi. By comparison, in this stage of simulation, the EIRP value was not mapped to. Normalized transmitted power of 1 W was set, resulting a 46.7 dBm EIRP correspondingly. In addition, the 3dB bandwidth of the BBox is 25° and that of the simulated UPA was 25°. It was then proved that the virtual pattern resembled that of the practical transmitter.

2.2.2 Ray tracing settings

Before carrying on to propagation simulations in ProMan interface, basic principles and some frequently used settings for this project are discussed in this section.

To begin with, ray tracing refers to the techniques depicting all possible ray paths between point-to-point transmitter and receiver pairs [28]. By applying such a function in ProMan, general settings are required regarding the transmitter, receiver, and computation methods.

Sectored sites are possible transmitters, where the operating frequency, transmitted power, position, and specific antenna patterns can be defined. Rotation of such a pattern can also be easily defined in this step.

As mentioned before, in this project, receivers are assumed to be isotropic. Therefore, only positions of them need to be defined and are then defined by the prediction surface and the resolution size.

Once the transmitter and receiver were defined, detailed ray tracing settings are required. To be clear and specific, standard ray tracing (SRT) was selected as the computational method for all the propagation level simulations in this work. Given such a method, path loss mainly consists of free space path loss (FSPL) and transmission loss of materials [29]. The losses are computed by the Fresnel coefficients as shown in the equations below.

$$\mathrm{FSPL_{dB}} = 20\log_{10} d + 20\log_{10} f + 20\log_{10}\left(\frac{4\pi}{c}\right) \tag{2.3}$$

Eq. (2.3) expresses FSPL in dB scale, where d represents the distance in meter, f is the frequency in Hz, and c is the speed of light in vacuum.

$$L_T = 20 \cdot log(|T_{12}| \cdot |T_{21}| \cdot |T_2|) \tag{2.4}$$

The transmission loss can be expresses as Eq. (2.4), where T_{12} and T_{21} is caused by the transition into and out of the material. T_2 refers to the magnitude of the transmission coefficient of such a material.

$$|T_{12}| = \frac{2}{\sqrt{1+\sqrt{\varepsilon'_{r2}+\varepsilon''_{r2}}+2\cdot(\varepsilon'_{r2}+\varepsilon''_{r2})^{\frac{1}{4}}\cdot\cos\left(\frac{1}{2}\arctan\frac{\varepsilon''_{r1}}{\varepsilon'_{r1}}\right)}} \tag{2.5}$$

$$|T_{21}| = \frac{2\cdot(\varepsilon'_{r2}+\varepsilon''_{r2})^{\frac{1}{4}}}{\sqrt{1+\sqrt{\varepsilon'_{r2}+\varepsilon''_{r2}}+2\cdot(\varepsilon'_{r2}+\varepsilon''_{r2})^{\frac{1}{4}}\cdot\cos\left(\frac{1}{2}\arctan\frac{\varepsilon''_{r1}}{\varepsilon'_{r1}}\right)}} \tag{2.6}$$

$$|T_2| = e^{-2\pi f d\cdot\frac{\mu_0\varepsilon_0\varepsilon'_r}{2}\left(\sqrt{\left(1+\frac{\varepsilon''_{r1}}{\varepsilon'_{r1}}\right)^2}-1\right)} \tag{2.7}$$

In the above equations,

ε'_{r2} and ε''_{r2} are the real and imaginary parts of the relative permittivity of the material, respectively.

ε'_{r1} and ε''_{r1} are those values of the environmental media. In cases of this project, free space is considered.

μ_0 is the permeability of free space in H/m.

f is the frequency in Hz.

d is the thickness of the material in meter.

Uncorrelated superposition of rays is specified in the simulation setup, meaning that the power values are summed.

2.2.3 Grid of beams

SRT was then applied to the database without furniture nor users to decide on the grid of beams.

To begin with, the phrase grid of beams stands for the set of possible beam steering patterns [30, 31].

As demonstrated in 2.1, a 3D database of the Snijderszaal without furniture nor users was created. Hence, propagation simulation can be conducted in ProMan interface. After importing the environmental database, sites or database can be created. In this case, a site with a one-antenna sector was simulated at the middle point on top of the entrance wall at (0.05 m, 4 m, 3 m). The exported far field pattern of the UPA was then applied, with a 1 W transmitted power.

It is clear that the receivers were defined as ideal receiving points based on the resolution rate. In this step, prediction of receiving power levels of a rectangular area was applied. The surface was defined as the XY-plane of the room at a height of 1 m, assumed to be the height of users' heads. The resolution grids were set to be 0.2 m $\times$ 0.2 m.

Due to limitations of uploading the patterns, beam steering was achieved by geometrical rotation of the radiation pattern. The rotating azimuth and elevation angles are defined by the line of sight (LOS) angles. Therefore, to define the possible patterns, the room was divided into rectangular grids. Within each of the grids, DL requirements were treated by steering the beam onto the central point of it. SRT simulations were conducted to define the range of grids.

To begin with, the grids were assumed to be uniform in the Y-direction, and thus non-uniformly defined by the power drop in the X-direction. The drop from the center to the edge of the grids was expected to be 3 dB regardless of FSPL.

As mentioned, the surface prediction of SRT generates discrete results regarding centers of resolution grids. Therefore, a matrix of FSPL values based on the distances of resolution centers to the transmitter was created. By adding such a matrix in the predicted power levels, path loss can be removed.

Eventually, 29 grids were generated. They were numbered and shown in Fig. 2.6a.

Contour lines of the 3 dB power drop from the centers were then plotted. By comparison, the small circles on horizontal sides showed that areas blocked by the pillars did not meet the expectation. Additionally, overlaps of contour lines were viewed in the front grids, meaning that such areas were over-divided. Despite the difference, in the central area of the room, where users were expected to be, the grids satisfied the design.

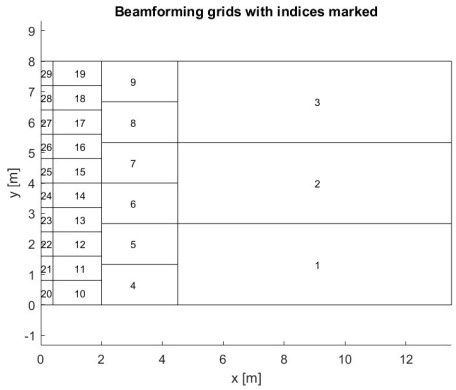

(a) Grids of the 29 scenarios

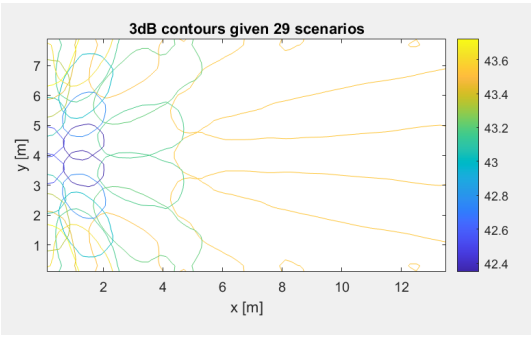

(b) 3 dB contours given the 29 centers

Figure 2.6: Comparison of contours and divided grids

With the grids defined, the beam steering angles can then be calculated. The exact values are presented in the appendix. In the following parts of the thesis, the simulations results using such patterns are numbered as the same. This kind of single simulation with a specific pattern in a specific pattern is called a scenario. Therefore, there are in total 29 scenarios for one database.

When it comes to coverage discussion, it is wanted that the received power levels in the whole room are similar. However, this is hard to achieve using a high directive antenna without beamforming. Taken scenario 2 and 26 of the database 1 for example, the received power levels in grid 26 for scenario 2 were around -50 dBm, while in scenario 26 increased to around 28 dBm. Such an increase in power justified the implementation of beamforming.

However, it is worth noting that although 29 patterns were created and collected in the grid of beams, they were just rotated versions of the broadside pattern. The phases of elements of the UPA remained unchanged. However, this is only true simulation wise. In the measurement stage, the BBox was fixed and beamforming was conducted by active excitation. Detailed information can be found in section 2.5. Therefore, with the implementation of broadside pattern in the simulations, discrepancies were expected on antenna gain and side lobe levels when it came to the measurement. Compensation was made in post-processing. Detailed information is given in section 2.5.

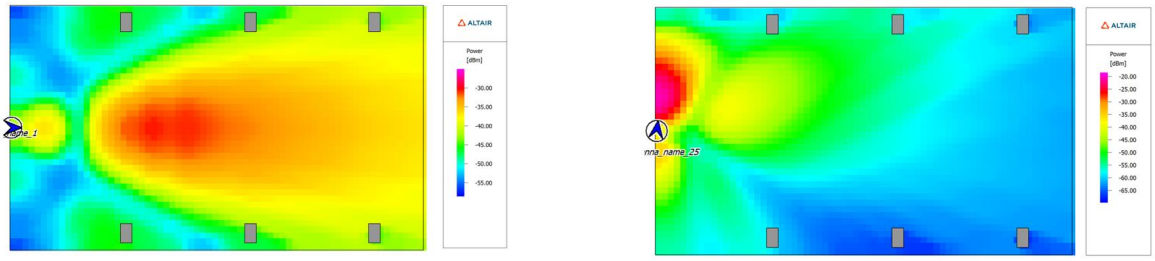

(a) Power distribution scenario 2 database 1

(b) Power distribution scenario 26 database 1

Figure 2.7: Two pictures side by side

2.3 Simulation setup and results

2.3.1 Distribution of objects

In this section, updates were made upon the model of the Snijderszaal by putting objects inside. Comparison among different propagation environments were conducted, stressing the importance of defining the details in the step of room simulation.

To be specific, similar methodologies were applied to both presentation and meeting scenarios. Compared to the empty room database, the first modification was put furniture inside. This distinguished the models of the presentation and the meeting scenario.

As it is hard to represent the actual shapes of the chairs and tables in the simulation, both of them were simplified into floating cuboids. The measured material properties of the seat surface and the tabletop were applied.

A chair was then 0.5 m $\times$ 0.5 m by size, and the material thickness was defined to be 0.05 m. It was place at z = 0.475 m to make the upper surface of it at 0.5 m high related to the ground.

Similarly, a table was defined by a cuboid of 1.2 m $\times$ 1 m $\times$ 0.1 m with the corresponding dielectric properties.

As shown in Fig. 2.1a and Fig. 2.8a, in total 6 rows of chairs were implemented. Each row had 6 chairs with a passageway in the middle. The distance between each row was set to be 1 m and the first row started at x = 2.5 m. Tables were not used in such a layout.

As when the Snijderszaal was used for a meeting, tables were placed jointly in a circle. However, in a practical case, there were tables of different sizes. The model was modified in the measurement section to more closely represent the actual environment. At this stage, to make the layout more uniform, tables were simulated as the same. In addition, for each table, only one chair and one user was considered. The central axes

were aligned.

After that, full user density was considered. This was achieved by creating human representing cuboids and placing them on the center of the the chairs. The complex permittivity of human skin at 26.5 GHz was applied. The seated users were placed facing the tables with a 0.2 m thickness, 0.5 m width and 0.8 m height. A standing person such as the presenter was defined by the same size but with a height of 1.8 m.

However, an issue occurred in this step. Combining the positions of the chairs and division of the grids, there were chairs placed on the border of two grids, resulting in ambiguity of beamforming. To avoid not knowing where to steer the beam, the full user density was defined with such chairs empty.

With the limited but still maximal number of users put in, comparisons were made to study the scattering effects of users.

Images depicting the databases except for the empty room in Fig. 2.3 are shown in Fig. 2.8.

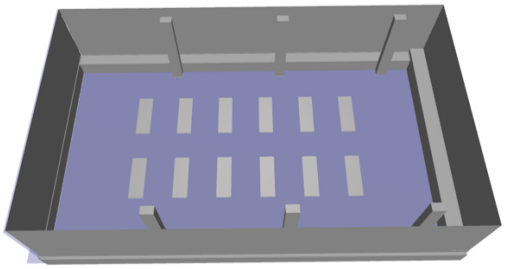

(a) Layout of the presentation usage without users

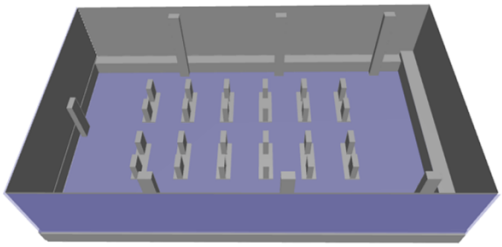

(b) Layout of the presentation usage with users

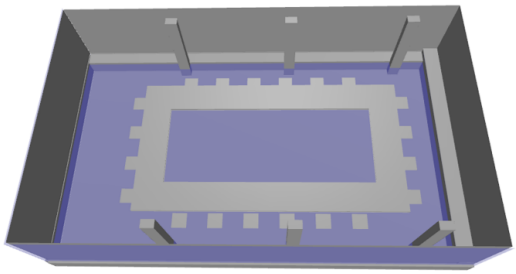

(c) Layout of the meeting usage without users

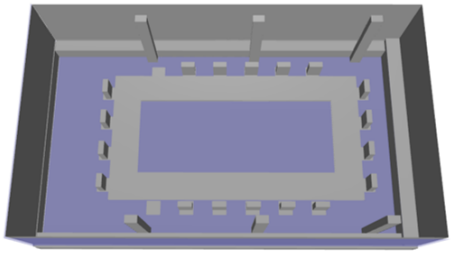

(d) Layout of the meeting usage with users

Figure 2.8: Indoor environments for propagation simulations

In the presentation usage, 24/36 seats were able to be occupied. Additionally, a presenter was created in the front of the room. In such a case, the presenter was considered not requiring any data, thus only being a part of the environment. By

comparison, the number of seats was reduced to 20 in the meeting usage, while only 2 seats were unavailable. Databases shown in Fig. 2.8a - (d) are numbered as database 2 - 4.

Table. 2.4 below shows the specific cases considered.

Grid index	1	2	3	5	6	7	8
Number of users (presentation)	4	8	4	2	2	2	2
Number of users (meeting)	6	2	6	1	1	1	1

Table 2.4: Number of users in each grid

Given the positions of UEs, only 7 patterns from the grid of beams were simulated. By applying the corresponding rotation angles, SRT simulations were conducted.

2.3.2 Simulation setups

In the ProMan interface, two types of prediction results can be generated. The first one is point prediction, where the received power levels at a specific point is generated by applying an isotropic receiver. The second one is surface prediction with a resolution. For each resolution grid, a point prediction is conducted to represent the whole grid [29].

Due to limitations of the simulation software, the beamforming scenarios were simulated independently. Therefore, it is assumed that each scenario lasts the same time, noting as a unit time. It is also assumed that the every user requires for the same amount of DL data. As a result, in order to satisfy the same DL requirement in a unit time for users at different locations, the transmitted power is modified.

It is worth mentioning that with an unchanged propagation environment and simulation method, the relation between received power levels and the transmitted power is linear in dB scale. This can be easily proved by looking at the loss formulas of Eq. (2.3 - 2.7).

Therefore, the maximal received power of all centers when 1 W was transmitted was selected as the target. Additional power was added when the beam is switched at other grids. Thus, the additional powers needed can be calculated by subtracting maximal received power by the other power levels. By adding such values, the modified transmitted powers were then obtained.

Point predictions were conducted in order to compute the amount of additional powers. Other results were based on surface predictions. Details of the initial simulations are presented in Table. 2.5.

To specify simulations setups, the simulation database, the required result type and

Simulation index	A	B	C	D	E	F	G
Database	1	2	3		4	5	
Required results	Surface prediction	Surface prediction	Surface prediction	Point prediction	Surface prediction	Surface prediction	Point prediction
Resolution rate [m]	0.2	0.2	0.2		0.2	0.2	
Beamforming scenarios	1,2,3, 5,6,7,8	1,2,3, 5,6,7,8	1,2,3, 5,6,7,8	1-29	1,2,3, 5,6,7,8	1,2,3, 5,6,7,8	1-29

Table 2.5: Initial simulations parameters

the resolution rate, and the applied pattern of each simulation are listed. Different simulations are named by alphabets to distinguish from the beamforming scenarios.

Simulation A focused on the scattering of an empty room of the Snijderszaal. As this was only for comparison with databases with furniture and users, the resolution rate and the beamforming scenarios were aligned to those with users.

For surface predictions, the general settings can be found in section 2.2.3. In most of the simulations, the prediction surface is at 1 m high with a resolution edge of 0.2 m. Additionally prediction surfaces were added to find the most exposed position on the most exposed user. However, this requires knowledge of further processing on the simulation results. Thus, detailed information is going to be included in section 2.4.1.

In addition, surface predictions were generated in simulation B and E, where no user was considered in the databases, but only beamforming scenarios of the potential users were considered. This also guaranteed the alignment of dataset dimensions, which made subtraction possible. For simulation C and F, similar simulations were conducted by replacing the databases to the ones with users inside.

Eventually, point predictions were conducted in simulation D and G. As no resolution rate is needed for such prediction, the blocks were left blank.

Received power at each user can be extracted from the surface prediction results, but in this stage, the difference among grids was simplified and quantified by comparing the received power at the centers. As might redundant, 29 scenarios were simulated. Starting with point predictions for grid centers, such power levels were considered to be representing the general receiving conditions of the whole grid.

As a result, the maximal received power levels were not included in the final beamforming scenarios. As demonstrated in Fig. 2.8b and 2.8d, no chairs were placed in the front of the room, where the small path loss leads to a large receiving.

To sum up, this section presents various databases of the Snijderszaal used in the indoor propagation simulations. With the positions of users defined in Table. 2.4, simulation scenarios were defined and SRT simulations were conducted afterwards. Following up simulations were conducted once the initial results were analyzed. They

are shown together with the processing of result in the next section.

2.4 Results and post-processing

In section 2.4.1, an additional section was carried out to show the necessity of refining the models. Comparison of different models was conducted to quantify the influence of placing objects inside the room. The general propagation simulations were conducted based on full user density scenarios of the presentation and meeting uses. Post-processing of these initial results is presented in section 2.4.2. After that, further simulation regarding the most exposed user was conducted and the results were analyzed in section 2.4.3 and 2.4.4. The latter can then be migrated to the full wave level human skin model simulation.

2.4.1 Difference among databases

To begin with, regarding all the 5 databases, surface predictions with the beam steering towards the UEs were generated. To quantify that, 7 patterns were applied and 2720 data points were generated for each scenario.

By exporting the data into ASCII format, predicted power levels in dB scale can be stored in matrices in MATLAB.

The first step is adding the calculated differences to the extracted power levels. The specific values are shown in the appendix. The total 29 scenarios were considered so that the maximal receiving centers were not of those user occupied grids. For presentation and meeting cases, the maximal received power levels were generated at the centers of grid 24 and 25, respectively.

By such simulations, the main aim is to find out how the propagation of wave is influenced by the modifications on the layout of rooms. First of all, the universal effect is studied by summing the resolution grids and averaging the scenarios. The expression of the averaged difference in dB scale is shown in Eq. (2.8).

$$\mathrm{D} = 10 \times log_{10}(\frac{1}{m}\sum_{j=1}^{m}\frac{\sum_{i=1}^{n}|\mathrm{P}_{2(i,j)} - \mathrm{P}_{1(i,j)}|}{\sum_{i=1}^{n}\mathrm{P}_{2(i,j)}}) \tag{2.8}$$

, where D stands for the difference ratio in dB scale. m is the number of beamforming scenarios. n is the index of exported power levels at different locations. P_2 stands for the power level of the updated databases. P_1 stands for the power level of the initial databases.

In this step, m = 7 and n = 2720.

The overall differences in dB scale are displayed in Table. 2.6. As they are ratios, no unit is applied.

P_1 \ P_2	2	3
3	-61.35	-61.19
4	-64.15	-63.84

Table 2.6: Overall difference among databases in dB scale

From the results, it can be seen as that the overall received power levels, or putting as the coverage was not strongly influenced by the addition of furniture and users. However, as the validation setup is spot measurement by placing a sensor to specific location, the point-wise difference is more of the concern than the averaged one. Due to the page limit, scenario 2 is selected to show such differences.

Similarly, 4 comparisons were made. The comparison was conducted by subtraction of the power levels in dB scale directly. Difference plots were made by taking the absolute values.

To begin with, the influence of furniture was considered. However, since they were simulated by floating cuboids, the influence is less visual at 1 m. In total 4 simulations were generated based on the 3 databases without users. The presentation usage one was given as an example in Fig. 2.9.

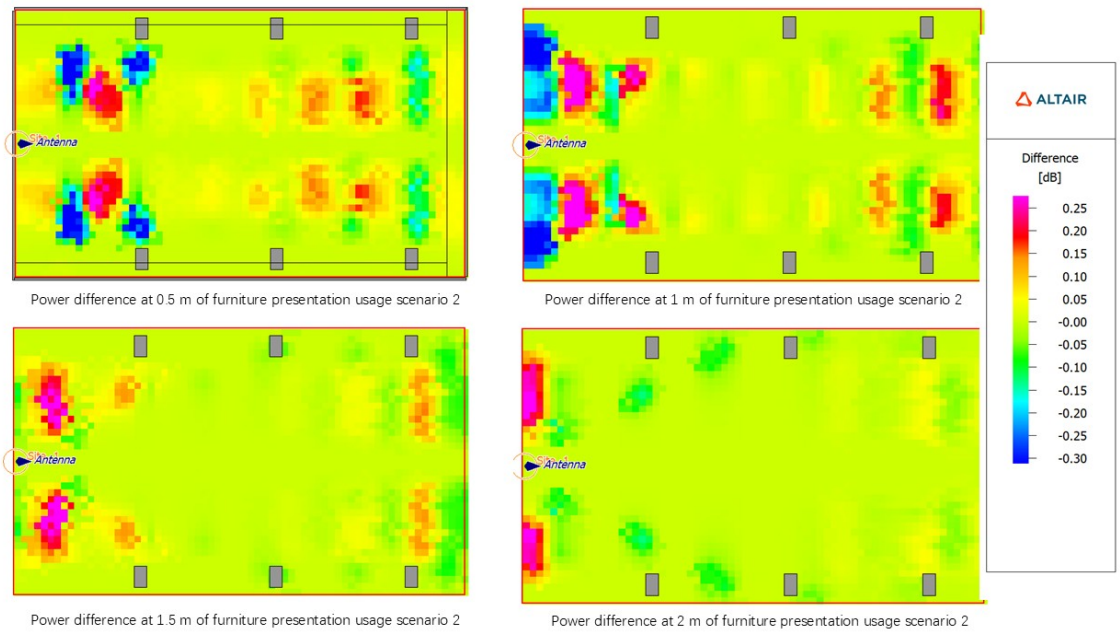

Figure 2.9: Power difference of furniture presentation usage scenario 2 various heights

Given the limitation that parts of users under the furniture were not considered, the simulation started from 0.5 m and went to 2 m with an increment of 0.5 m. The

difference plots showed that although the difference levels tend to be larger nearby the furniture, they are generally small.

By contract, the influence of the users are more obvious.

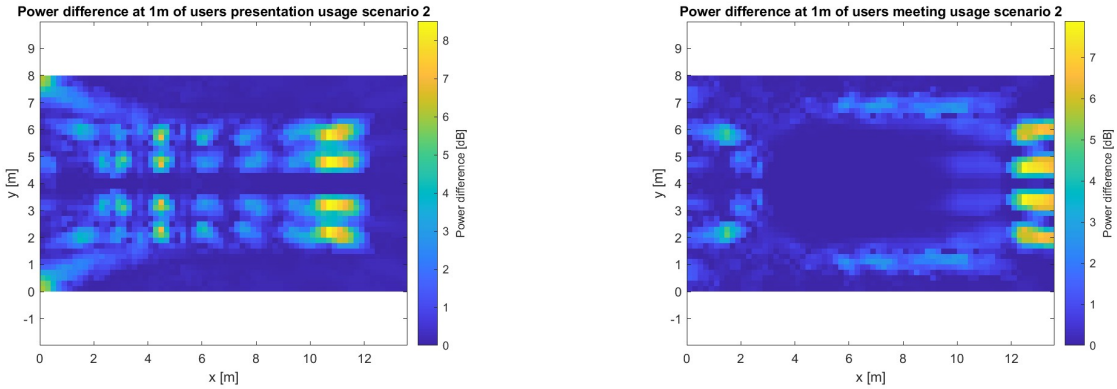

(a) Power difference at 1 m of users presentation usage scenario 2

(b) Power difference at 1 m of users meeting usage scenario 2

Figure 2.10: Difference of users at 1 m scenario 2

It can be seen from the results that the point power differences around users were considerable. Moreover, the influence of the users in the steered grid is relatively higher than those in the other grids. This provided a strong proof that refinement of the indoor databases is a necessary step, especially for users. Meanwhile, as the meeting scenario is more complicated, the furniture indeed has a larger influence.

As a result, the presentation and meeting room layouts with users are then chosen as the final databases for the following indoor propagation simulations. Some initial prediction results are already acquired in simulation C and F. The next section will give a detailed illustration on how these data are processed.

2.4.2 Post-processing of simulation results

As stated above, the weights of the grid user density are already applied to the simulation results. In this case, the scenario-average-mostly exposed users can be found by comparing the received power levels of them.

The results were power levels of the XY-plane at the height of 1 m. Through previous processing, namely modification of the transmitted power and averaging of 7 beamforming scenarios, the receiving conditions are shown in Fig. 2.11a and Fig. 2.11b.

In such results, several data points can be extracted given the area a user occupies. It is considered that in this stage, the resolution is sufficient to identify the most exposed user among all users.

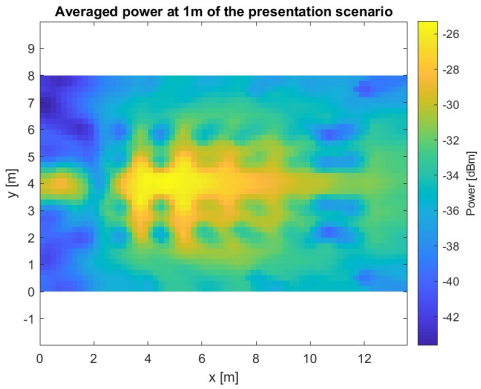

(a) Averaged power at 1 m presentation usage

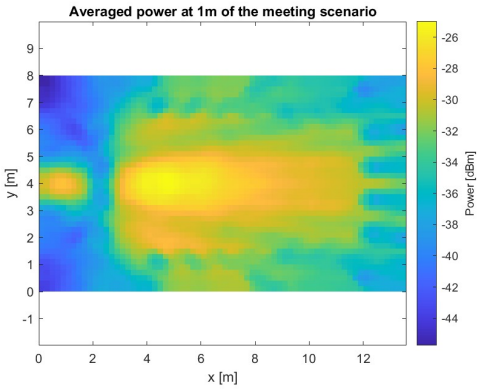

(b) Averaged power at 1 m meeting usage

Figure 2.11: Averaged power distributions at 1 m

The similar averaged power levels also proves the success of the transmitted power modification.

As a user was surrounded by 10 resolution grids, by comparing the maximum values of each user, the most exposed user can be found. Once the two users were found, they were marked on the Snijderszaal diagrams by a red pentacle on the chair.

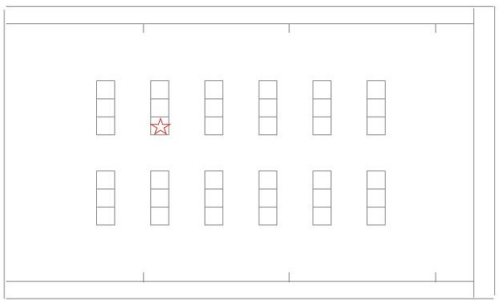

(a) Maximally exposed user presentation

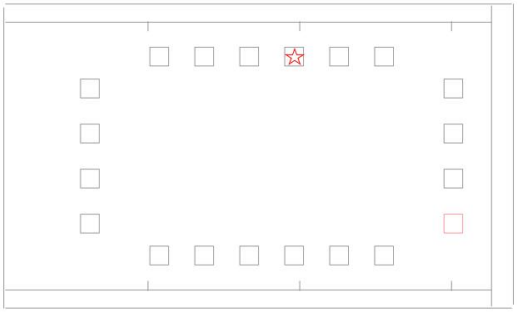

(b) Maximally exposed user meeting

Figure 2.12: Maximally exposed users in presentation and meeting scenarios

As the indicator for the final exposure assessment is a value of surface power density, the most exposed points upon the users are required as well. In order to find the incident angle regarding that specific positions yet not known, simulations were conducted additionally by adding user-defined prediction surfaces in the database.

2.4.3 Single user simulations

Combined the positions of the two users and the results in Fig. 2.11, among all 6 surfaces of the cuboids representing users, 2 surfaces were selected.

For the presentation scenario, the left YZ-plane was selected at x = 4.15 m. By contract, for the meeting scenarios, the lower XZ-plane was chosen at y = 6.55 m. After modifying the databases with the prediction planes, the resolution was also reduced to 0.1 m to better suit the size of a user.

In this stage, 7 surface prediction results were generated for each person corresponding to the beamforming scenarios. Therefore, 7 maximal power values were found on the surface and 7 incident angles can be calculated.

The angles are again calculated as those of the LOS rays, while the power levels are the uncorrelated superpositions of all rays.

The positions and incident angles are listed in the Table. 2.7

Beamforming scenarios		1	2	3	5
Presentation	Positions (y, z)	(4.55, 1.25)	(4.55, 1.25)	(4.95, 1.25)	(4.95, 1.25)
	Azimuth ∘	7.640	7.640	13.046	13.046
	Elevation ∘	22.930	22.930	22.578	22.578
Meeting	Positions (x, z)	(7.9, 0.55)	(7.9, 0.55)	(7.9, 1.05)	(7.9, 0.85)
	Azimuth ∘	4.008	4.008	4.008	4.008
	Elevation ∘	17.293	17.293	13.918	15.281
Beamforming scenarios		6	7	8	
Presentation	Positions (y, z)	(4.55, 0.75)	(4.95, 0.55)	(4.95, 0.85)	
	Azimuth ∘	7.640	13.046	13.046	
	Elevation ∘	28.542	30.205	27.060	
Meeting	Positions (x, z)	(7.5, 1.05)	(7.9, 0.85)	(7.9, 0.75)	
	Azimuth ∘	4.222	4.008	4.008	
	Elevation ∘	14.630	15.281	15.956	

Table 2.7: Maximal power positions and incident angles

However, the real shape of a human body is different from a cuboid. This mainly has an influence on the simulation as human body has no arris. The multi-layer skin model is also a cuboid. This leads to an issue that even the size of the skin model is too small to be considered as on the flat surface in the propagation simulation, applying the obtained incident angles shown in Table. 2.7, the simulation will calculate in that way. Therefore, to represent the situation where the ray incidents a sufficiently small area of a user, only elevation angles were considered in the latter simulations.

2.4.4 Indoor propagation results

Given the excitation method As mentioned before, the receivers were by default isotropic. Therefore, the effective antenna area of them at 26.5 GHz can be computed using Eq. (2.9).

$$Ae = \frac{(\frac{c_0}{f})^2 G}{4\pi} \tag{2.9}$$

Ae stands for effective cross-section area in m^2.

c_0 is the speed of light in vacuum in m/s.

f is the frequency in Hz.

G is the gain and equals 1 here.

Therefore, the simulated results can be converted to power density by:

$$P_d = \frac{P}{Ae} \tag{2.10}$$

, where P_d stands for surface power density in W/m^2, P stands for power in W, and Ae stands for effective cross-section area in m^2.

The maximal received powers density in time domain are then plotted with an increasing ascending order of the beamforming indices.

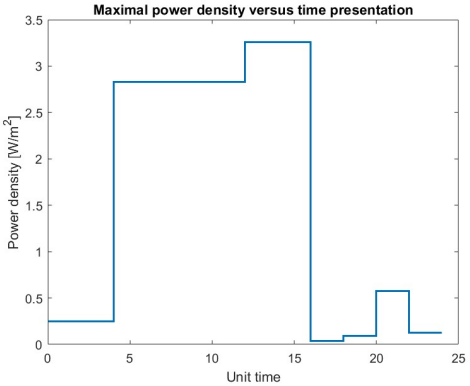

(a) Maximal power density versus time presentation

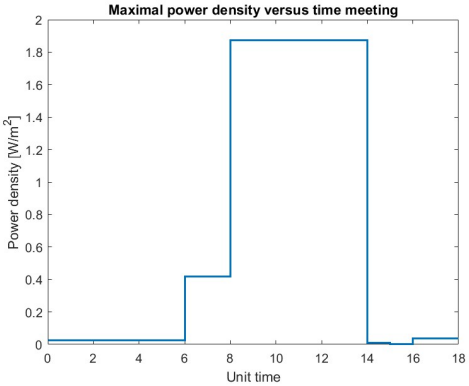

(b) Maximal power density versus time meeting

Figure 2.13: Final results of propagation simulations

Detailed steps of using such results as the excitation sources in the skin model simulation are presented in section 3.2.

2.5 Measurement

This section is devoted to explain how a measurement of meeting scenarios was conducted. Three parts are included in this section, namely actions in advance of the measurement, the measurement, and analysis of the results.

2.5.1 Preparation

Preparations were conducted to perform the final measurement, including calibration of devices, modification on simulations, and 3D printing holders for the BBox and the sensor.

2.5.1.1 Calibration of devices

To begin with, the BBox has a typical effective isotropic radiated power (EIRP) of 41.5 dBm at 28 GHz when used as a transmitter [27]. Given the fact that the central frequency of this work is 26.5 GHz, an additional EIRP measurement was conducted in an anechoic chamber.

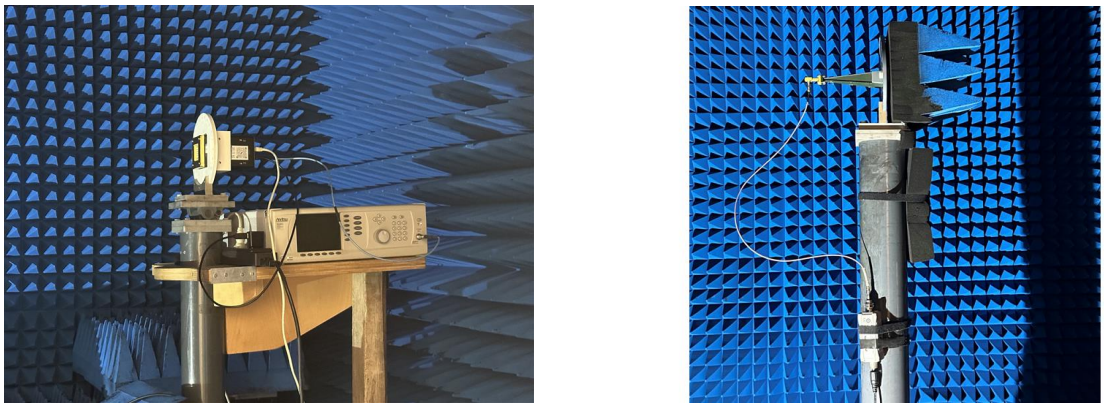

(a) EIRP measurement transmitting side

(b) EIRP measurement receiving side

Figure 2.14: Setup of the BBox EIRP measurement

As shown in Fig. 2.14, the BBox was used as a transmitter and a horn antenna was used as the receiver. Therefore, the BBox was connected to a power supply, an RF generator at 26.5 GHz, and a computer with its software control. The horn antenna was connected to a powermeter. The measured power levels was read by a MATLAB code on the computer that was connected to the powermeter.

As written in the handbook, the typical input power is 2 dBm [27]. Therefore, with a cable loss of approximately 3 dBm, the generator was set at 5 dBm. In addition, the gain of the receiver was measured to be 24 dB.

Index	1	2	5	6	7	8
Azimuth ∘	119	90	48	73	107	132
elevation ∘	9	10	24	30	30	24

Table 2.8: Beam steering angles measurement

With a distance of 3.6 m, the transmitted power can be easily calculated by Eq. (2.3).

The received power was -30.4 dBm, resulting in an EIRP of 22.8 dBm. However, in a feasibility test with a horn antenna and a spectrum analyzer, and in the final test, the obtained power was around 20 dB higher than the expectation. Therefore, there lied a huge error in the chamber measurement. Eventually, the typical EIRP at 28 GHz from [27] was used in the simulations.

2.5.1.2 Modification of simulations

In addition to the modification of the transmitted power, the layout of the furniture in the database was also changed to match the measurement scenarios.

Firstly, due to the limit of subjects, only 6 people were placed into the room. While a lower user density is unavoidable, efforts were taken to maintain the beamforming scenarios as much as possible. Therefore, one user was placed into each grid. However, there was still a lack of a user. As the relatively high exposed positions are more concerned, one of the 1-3 grid was considered to be set as empty. Due to the symmetry of grid 1 and 3, eventually grid 1, 2, 5, 6, 7, 8 were occupied.

Secondly, there were two types of tables in the room. The ones that were placed at the long end were 0.8 m × 1.6 m, and those placed at the short end were 0.7 m × 1.8 m. Both of them are 0.8 m high. Therefore, the sizes of tables were modified. They were simulated as a spliced ring-shaped board in the environmental model.

Meanwhile, to make room for the transmitter setup, one table was removed on each side, resulting in 18 tables and chairs in total.

The final layout of the propagation environment for the measurement is shown in Fig. 2.15.

Eventually, it was not possible to fix the BBox on the ceiling. A ladder was used on a table to support it. This led to a change of position of the antenna to (0.32 m, 4.4 m, 2.45 m). Corresponding modification was made, along with that on the transmitted power.

Once the positions of the users and the transmitter were determined, the steering angles were computed.

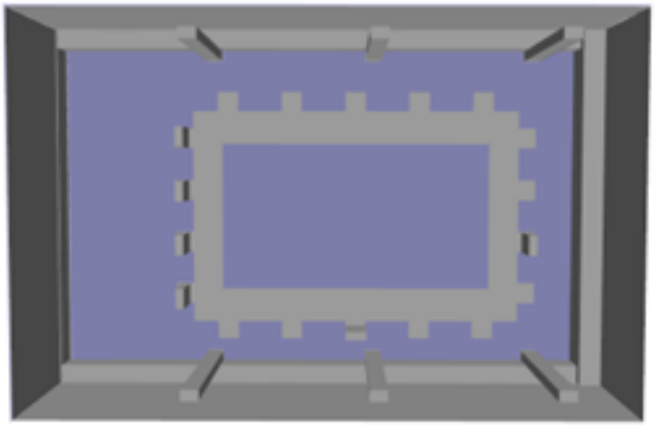

Figure 2.15: Database for measurement scenario

This simulation also aimed at finding proper positions to place the sensor. Given the a table height at 0.8 m, a holder was designed to make the sensor 0.2 m above the table. Thus, surface predictions at 1 m were then conducted and processed.

As the modification of transmitted power was not applied. Meanwhile, the BBox was used as an active phased array in the measurement so that an error was introduced by the scan loss.

The transmitted power in the simulation was selected as the EIRP value, thus only the differences of the directivities at the steered angles to that of the broadside were needed. Such values regarding angles in Table. 2.8 were computed in MATLAB. Additionally, as mentioned above, this was conducted by linear addition to the acquired data.

A plot of the averaged power distribution at 1 m high is depicted in Fig. 2.16.

To vary the measurement cases, 3 positions were selected to put the sensor and then measurements were conducted individually. The selection also considered the fact that the holder needs to be place on a table.

The selected measurement locations were marked by * in red, magenta and white, with estimated large, medium and low received power levels respectively. They are indexed as location 1: (3.75 m, 5.45 m, 1 m), location 2: (7.45 m, 6.85 m, 1 m), location 3: (11.05 m, 4.65 m, 1 m).

The expected power levels versus time are shown in the figure below.

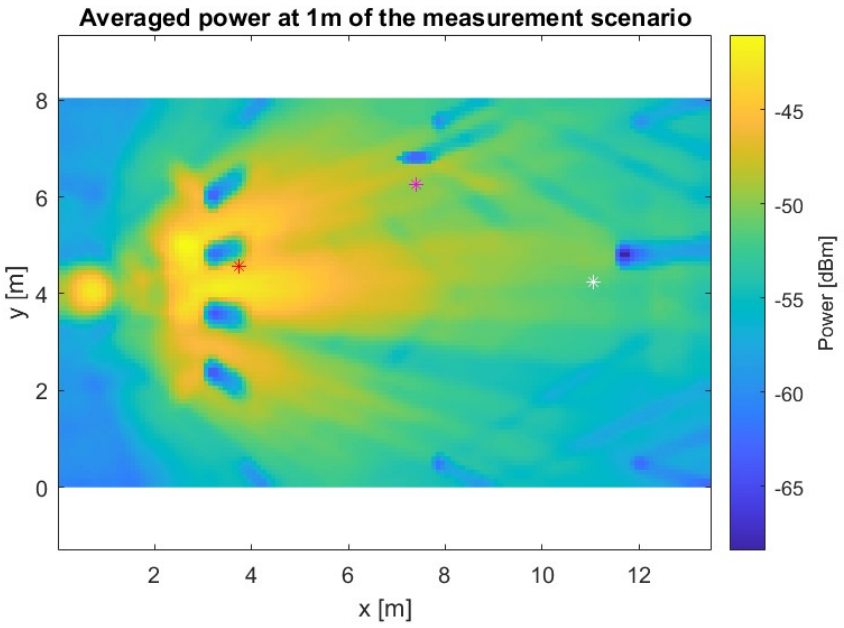

Figure 2.16: Averaged power measurement with sensor positions marked

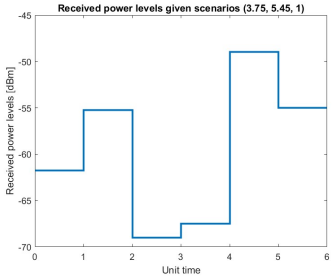

Figure 2.17: Simulation results location 1

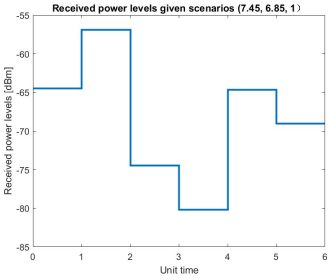

Figure 2.18: Simulation results location 2

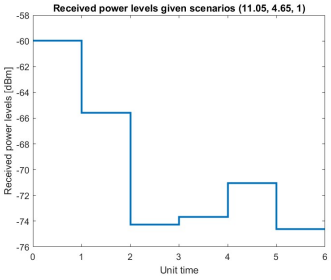

Figure 2.19: Simulation results location 3

Figure 2.20: Simulation results of the measurement setup

2.5.1.3 3D-printed sensor holder

A lens-based high-sensitivity 5G mm-Wave EMF sensor was used for the measurement. Such a sensor is dual polarized, allowing captures of both polarizations of incoming waves. When it comes to over-the-air (OTA) conditions, the broadside direction of the sensor needs to be aligned with the incoming ray. Therefore, as there was an elevation angle of the LOS ray to be measured, it was crucial to keep the sensor at an orthogonal angle.

Holders were designed based on the measurement positions. However, due to limi-

tation only one of them were 3D printed, introducing an error up to 10 ∘.

The holder with the sensor mounted on it is shown in 2.21. A slope with the calculated angle was supported by 2 pillars, with holes to screw the sensor on. An hollow is created behind the sensor, allowing connection to the feed.

Figure 2.21: The sensor mounted on the holder

2.5.2 Measurement setup

The devices needed for the measurement are listed below.

- The BBox, a laptop with the software to control it, an RF generator for it, an Ethernet cable to connect it to the laptop, a cable to connect it to the generator, and a power cable.

- The sensor, a laptop to read the data from it, a bias supply for it, a holder to support it, and wires.

- A ladder and a holder on the ladder to place the BBox.

To begin with, the BBox was mounted on a ladder located at (0.32 m, 4.4 m, 2.45 m). It was connected to a generator at 26.5 GHz, with an output of 5 dBm of power. An Ethernet cable connected it to a computer, from which commands of steering angles were sent.

In the room, 6 subjects were seated as shown in Fig.2.15. The sensor was placed at location 1, connecting to a bias supply and a laptop used to control it and read data out.

A person was standing next to the BBox. Once a pair of beamforming angles in Table. 2.8 was applied, readouts of the sensor were gathered. This step was repeated

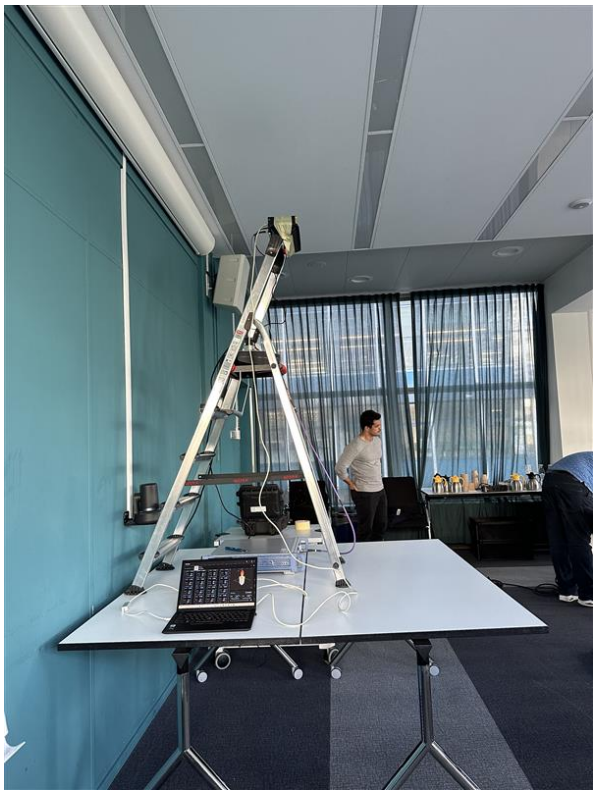

Figure 2.22: The transmitter setup of the measurement

Figure 2.23: The measurement setup

6 times for the set of angles, after which the sensor was moved to the next location and the same measurements were carried out. As a results, 18 datasets were collected,

regarding 6 beamforming scenarios each of the 3 locations.

2.5.3 Results and analysis

Dynamic readouts were acquired. The readings from the sensor were stationary for each beamforming scenario, proving the stationary assumption. Therefore, the measured power levels of each scenario were averaged in post-processing, generating a single value.

By using such a value to represent the power level of a unit time, the measurement was compared to the simulation.

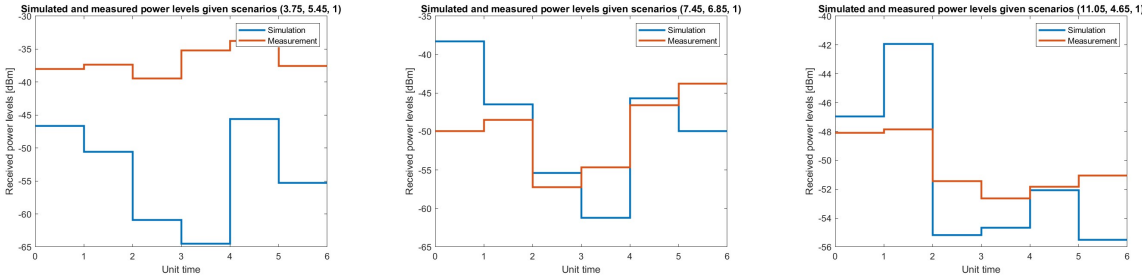

(a) Measurement versus simulation location 1

(b) Measurement versus simulation location 2

(c) Measurement versus simulation location 3

Figure 2.24: Propagation simulation results and measurements at three locations

Two reasons are considered for the discrepancy, namely the difference in the simulated antenna pattern and the practical antenna, and the error in positions of the sensor.

To begin with, a 3D far field file is required by the propagation simulation software. This made importing the measured BBox pattern impossible. However, with half wavelength elements and half wave-length spacing, the simulation UPA was ideal, leading to discrepancies of side lobe values.

The broadside pattern of the BBox is measured in the Dome The measurement setup and the results are displayed in the appendix. From the measurement, a cut can be made at phi = 0. The normalized plot was generated and compared to that of the simulated pattern from CADFEKO.

As shown in Fig. 2.25, the simulated pattern has lower null levels compared to that of the BBox. This results in small received power level in simulation such as that between t = 3 and t = 4 in Fig. 2.24a, while in the measurement such phenomena were not observed. Therefore, the discrepancy of the antenna patterns is the main reason for the differences between simulation and measurement.

Meanwhile, the simulated power levels were point prediction values at specific lo-

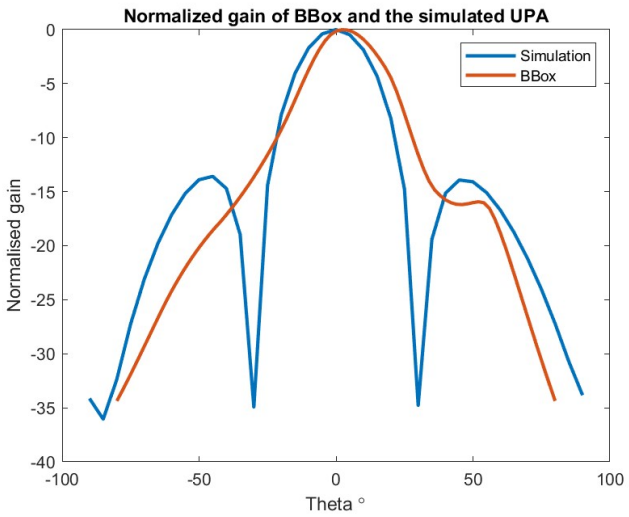

Figure 2.25: Comparison between broadside patterns of the BBox and the simulated UPA

cations. Much higher accuracy is needed to align with such values. However, such an error was not able to quantify.

3 Multi-layer skin model

3.1 Multi-layer skin model

To begin with, as the penetration depth decreases with an increasing frequency, at 26.5 GHz, it is considered that most of the exposure is absorbed in the skin cells.

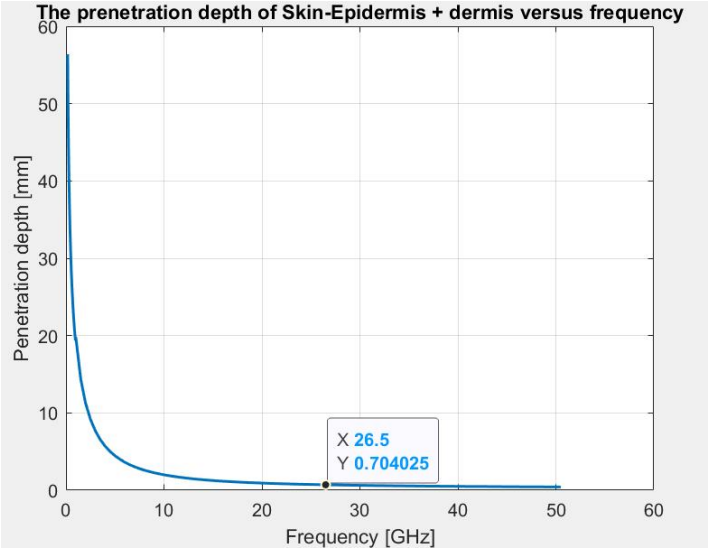

Figure 3.1: Penetration depth of human skin versus frequency

Considered as a homogeneous material, general dielectric properties are applied for skin-epidermis and dermis tissues [9]. With such values, the penetration depth of human skin versus frequency can be computed. Fig. 3.1 shows that from low frequency ranges (below 6 GHz) to the operating frequency of this work, the penetration depth drops hugely.

Therefore, with a 1.5 mm thickness of the skin model, it is safe to say that at this stage, a simulation limited within the skin layers can represent the overall exposure of a human.

The multi-layer skin model consists of 6 components in CST studio, namely the stratum corneum, middle epidermis, inner epidermis, dermis, blood vessel and sweat duct. As shown in Fig. 3.2, curves were inserted to model shape of cells. User-defined materials were applied to different layers [9, 32, 33, 34, 35]. It is 0.4 mm $\times$ 0.4 mm $\times$ 1.5 mm by size.

Layer	ϵ_r'	$\sigma'[S/m]$
Stratum cornuem	17.41	24.78
Sweat duct	23.20	0.01
Middle epidermis	16.95	19.61
Inner epidermis	16.95	19.61
Dermis	14.95	21.41
Blood vessel	25.03	41.27

Table 3.1: Dielectric constants of the skin layers

In addition, the blood vessel was inserted in the middle of the epidermis layer. The sweat duct was represented by linear spiral, where ionized water was considered so that a fairly small conductivity was assigned to the material.

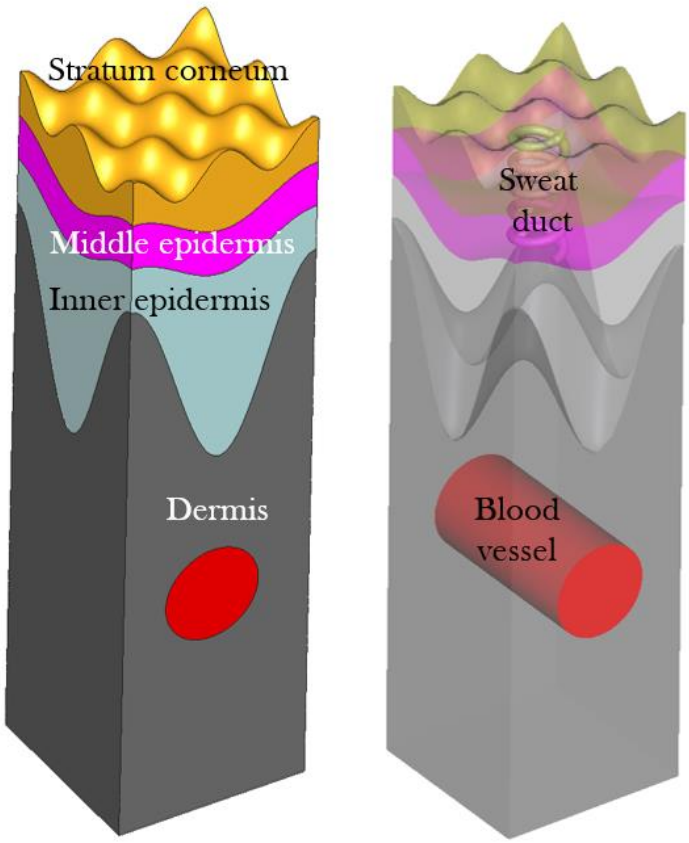

Figure 3.2: Multi-layer human skin model

3.2 Simulation setup

For each unit of time, a user in the room requires data and the beam pattern is then switches to the grid of the user. Although the DL requirements are considered equiva-

lent for each user, the total exposure levels differ. Therefore, the most exposed person among all users was selected. Once the user was chosen, for each beamforming scenario, the point of the largest power density on the user and the LOS angle from the antenna to it were extracted. Such values were used as the averaged power density of the incident wave, and the incident angle.

To align with the propagation simulations, static simulations were hence conducted in CST. The incident angles were set directly as the scan angles, while the power levels are scaled in post-processing. In total there are 14 simulation, consisting of 7 beamforming scenarios of the presentation and meeting usage each. The simulation was conducted based on the following designs.

- Floquet ports: stimulated at 26.5 GHz, TE and TM modes, 0.5 W transmitted power uniformly distributed on the XY-plane area of the skin model.

- Boundary conditions: unit cell setting for X and Y direction, open at Zmin (starting position of the skin model), and open with space at Zmax.

- Scan angles: elevation angles in Table. 2.7 were applied.

- Field monitors: SAR, power flow and E-field monitors at 26.5 GHz were applied to obtain the volume power densities.

- Mesh: default settings of the hexahedral type were applied.

- Solver: frequency domain solver from 26 to 27 GHz

- Post-processing: 3D integral of selected solids were conducted to obtain the absorbed power in each layer.

By these simulations, the overall observed power of the skin model is acquired. Due to the periodic boundaries, the surface power density results are the same as enlarging it to 4 cm^2.

3.3 Results and discussion

By various simulation in CST studio, the absorbed power of the whole layered skin model can be obtained and shown in Table. 3.2. By dividing the transmitted power, namely 0.5 W by such values, the normalized absorbing rates of the skin model at these incident angles are computed.

According to [3], at 26.5 GHz, the exposure is assessed by the surface power density absorbed. Therefore, by normalizing the absorbed power to the transmitted power of the floquet ports, the absorbed surface power density is calculated by:

	1	2	3	5	6	7	8
Presentation	0.2384	0.2384	0.2383	0.2383	0.2311	0.2288	0.2331
Meeting	0.2431	0.2431	0.2455	0.2446	0.2450	0.2446	0.2441

Table 3.2: Absorbed power in the skin model [W]

$$P_{d,a} = \frac{P_a}{P_t} \cdot P_d \tag{3.1}$$

, where $P_{d,a}$ is the absorbed surface power density, P_a is the absorbed power of the skin model, P_t is the transmitted power of the floquet ports, and P_d is the power density from the propagation simulation, also consider as the power that should be transmitted to the skin model.

The exposure predictions of the most exposed users in time domain are shown in Fig. 3.3.

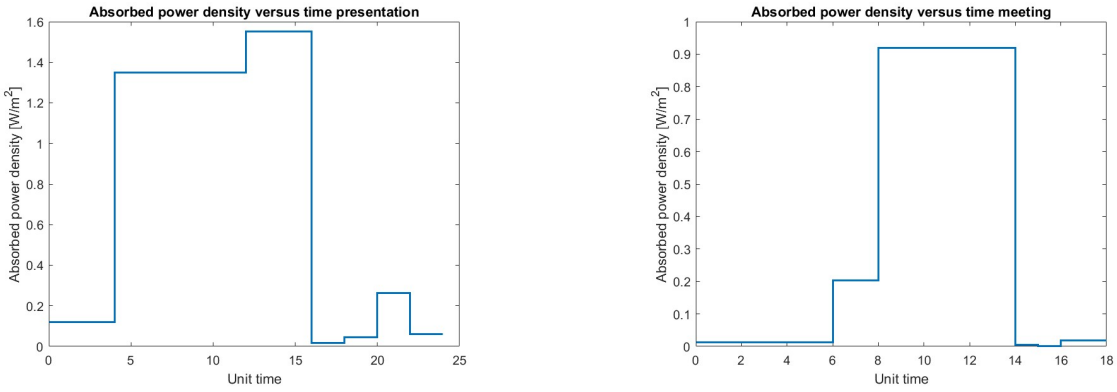

(a) Exposure versus time presentation

(b) Exposure versus time meeting

Figure 3.3: Exposure assessment

The predicted exposure values for both scenarios are well below the regulation of 20 W/m^2. When used for a presentation, the room is more crowded. This leads to a potential issue that relatively high exposed scenarios might be dominant in time.

In addition, the damage to the RBC is more concerned biologically. Although the position of the blood vessel is 0.9 mm underneath the top of the skin, it can be seen in the E-filed results that the power does not fully decay before the vessel.

Maximums on the cut planes are 85.7 and 77.3 dB (V/m). Despite the considerable decrease, the blood vessel is still exposed. In addition, in biologic experiments, the RBCs are exposed to EMF directly [36]. This makes it important to assess the realistic EMF exposure level of specific structures of the skin model.

Although the electromagnetic indicator of exposure changed surface power density

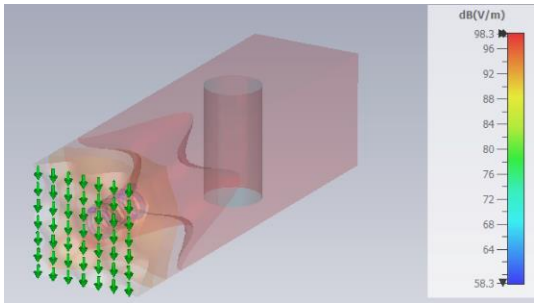

(a) E-field distribution before entering skin

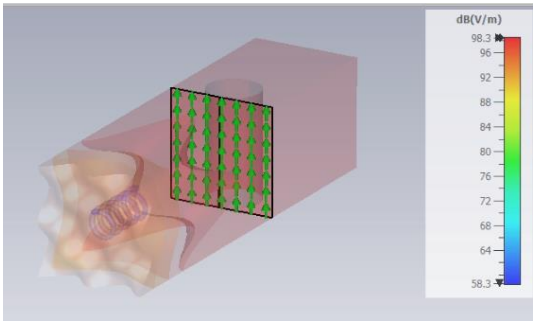

(b) E-field distribution before entering blood vessel

Figure 3.4: Decay of field strength from top of the skin to the blood vessel

above 6 GHz, the specific energy absorption rate (SAR) is still used to quantify the exposure level in biologic field. According to [3], the local exposure level is represented by the SAR over a 10 gram cuboid mass, and thus noted as SAR_{10}. With the periodic assumption, the value calculated from the blood vessel part in this model is representative and comparable.

$$SAR = P_a \cdot \rho \tag{3.2}$$

As shown in Eq. (3.2), the SAR is calculated by multiplying the absorbed power with the mass density of blood, which is 1060 kg/m^3 [37].

As shown in Table. 3.3, the absorbed powers differ very little and are already way below the regulation, only one simulation is taken for example. Thus, the one with the maximum overall received power, as beamforming scenario 3 of the meeting usage is chosen.

The same scaling is applied as in Eq. 3.1. Thus, the SAR of the blood vessel regarding the propagation scenario is then calculated by:

$$SAR_{m3} = \frac{P_a \cdot P_d \cdot S \cdot \rho}{P_t} \tag{3.3}$$

, where P_a is the absorbed power by the blood vessel, P_d is the power density extracted from the propagation simulation, S is the area of the floquet port, and ρ is the mass density of blood. As the wave is propagating along Z-axis, the XY-plane area of 0.4 mm $\times$ 0.4 mm is applied.

As shown in Fig. 3.5, approximately 0.01 W is absorbed in the blood vessel. The calculated value is hence 0.77 W/kg. Due to the fact that there is no regulation of such a quantity above 6 GHz, that below 6 GHz was used. The exposure level of the blood vessel is well below that of the regulation as 100 W/kg [3].

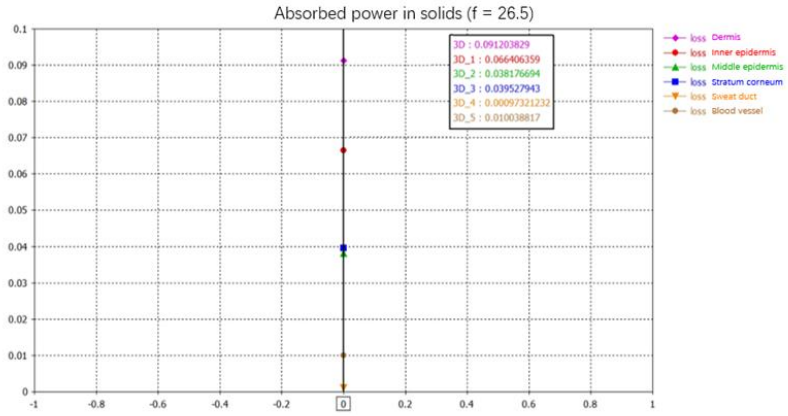

Figure 3.5: Absorbed power level in different skin structures

Due to the scalable feature, the frame can also be used to assess the exposure level of the blood vessel by modifying the transmitted power. Moreover, as such exposure value is calculated at the blood vessel, it is relatively more realistic for biological experiments than those at other parts of body.

4 Conclusion

This thesis presented a comprehensive methodology for assessing EMF exposure in 5G FR2 indoor scenarios with beamforming transmitters by integrating propagation-level simulations with a layered biological skin model. Measurements of material permittivity ensured realistic environmental databases, while ray-tracing simulations quantified the variations in power density across different user scenarios. These results were successfully combined to a multi-layer skin model to simulate localized energy absorption rates. The findings confirmed that even under maximum user density conditions, the predicted exposures remain far below international safety guidelines, while also revealing that beamforming introduces user- and scenario-specific variations that must be considered in exposure assessment.

The main contributions of this work include:

A validated workflow that links indoor propagation analysis to skin-level EMF absorption.

The first integration of ray-tracing results with multi-layer biological modeling in 5G FR2 exposure studies.

Experimental verification using practical measurement campaigns to support simulation results.

Future work should extend this framework to a full body human model where more complicated wave propagation mechanisms can be studied. Overall, the thesis proposes a new method to assess the EMF exposure of 5G FR2 band in indoor environments.

Bibliography

[1] J. Salvatore, "Electromagnetic fields," in *Encyclopedia of Toxicology (Third Edition)*, third edition ed., P. Wexler, Ed. Oxford: Academic Press, 2014, pp. 316–319. [Online]. Available: https://www.sciencedirect.com/science/article/pii/B9780123864543006035

[2] R. Goodman and A. S. Henderson, "Some biological effects of electromagnetic fields," *Bioelectrochemistry and Bioenergetics*, vol. 15, no. 1, 1986.

[3] International Commission on Non-Ionizing Radiation Protection (ICNIRP), "Guidelines for limiting exposure to electromagnetic fields (100khz to 300ghz)," *Health Physics*, vol. 118, no. 5, p. 483–524, 2020, pre-print published March 2020; supersedes 1998 guidelines.

[4] M. Leeman, R. Wydaeghe, J. van der Straeten, S. Goegebeur, G. Vermeeren, and W. Joseph, "City-scale spatio-temporal modeling of 5g downlink exposure of users and non-users by ray-tracing in a real urban environment," *IEEE Access*, vol. 13, pp. 30 894–30 906, 2025.

[5] M. Celaya-Echarri, L. Azpilicueta, F. A. Rodríguez-Corbo, P. Lopez-Iturri, V. Ramos, M. Alibakhshikenari, R. M. Shubair, and F. Falcone, "Towards environmental rf-emf assessment of mmwave high-node density complex heterogeneous environments," *Sensors*, vol. 21, no. 24, p. 8419, 2021.

[6] E. Chiaramello, M. Bonato, L. Fiocchi, G. Tognola, M. Parazzini, S. Ravazzani, and P. Ravazzani, "Radio frequency electromagnetic fields exposure assessment in indoor environments: A review," *International Journal of Environmental Research and Public Health*, vol. 16, no. 6, p. 955, 2019. [Online]. Available: https://www.mdpi.com/1660-4601/16/6/955

[7] F. Schettino, N. Petroulakis, M. Chortis, N. Karamolegkos, M. Simk
ø, M.-O. Mattsson, E. Soudah, M. D. Migliore, G. Panariello, D. Pinchera, M. Lucido, J. Bolte, E. Korkmaz, V. Theodorou, D. Laskaratos, A. Schiavoni, M. Spirito, F. V. Marcos, L. Colussi, A. Paragioudakis, M. Pruppers, and M. Velghe, "D2.2: Emf technologies and new exposure patterns," NextGEM – Next Generation Integrated Sensing and Analytical System for Monitoring and Assessing Radiofrequency Electromagnetic Field Exposure and Health, Tech. Rep., Deliverable D2.2, Work Package 2, Task T2.2 D2.2, Apr. 2023, contractual due date 30 April 2023; Actual submission date 30 April 2023; Lead Beneficiary: Università degli Studi di Cassino e del Lazio Meridionale; Public report. [Online]. Available: https://www.nextgem.eu/wp-content/uploads/2024/07/D2.2-EMF-Technologies-and-new-exposure-patterns.pdf

[8] S. Deng, M. K. Samimi, and T. S. Rappaport, "28 ghz and 73 ghz millimeter-wave

indoor propagation measurements and path loss models," in *2015 IEEE International Conference on Communication Workshop (ICCW)*, 2015, pp. 1244–1250.

[9] National Institute of Information and Communications Technology (NICT), Electromagnetic Compatibility Laboratory, "Data of dielectric measurements – skin-epidermis + dermis," NICT website, March 2023, database of relative complex permittivity and conductivity of skin tissue (epidermis and dermis), measured at 30–37°C. [Online]. Available: https://www2.nict.go.jp/cgi-bin/202303080003/public_html/index.py/measurements/Skin

[10] M. U. Sheikh, F. Ghavimi, K. Ruttik, and R. Jäntti, "Analysis of indoor solutions for provision of indoor coverage at 3.5 ghz and 28 ghz for 5g system," in *2019 26th International Conference on Telecommunications (ICT)*, 2019, pp. 340–345.

[11] B. Ai, K. Guan, R. He, J. Li, G. Li, D. He, Z. Zhong, and K. M. S. Huq, "On indoor millimeter wave massive mimo channels: Measurement and simulation," *IEEE Journal on Selected Areas in Communications*, vol. 35, no. 7, pp. 1678–1690, 2017.

[12] J. Li, B. Ai, R. He, K. Guan, Q. Wang, D. Fei, Z. Zhong, Z. Zhao, D. Miao, and H. Guan, "Measurement-based characterizations of indoor massive mimo channels at 2 ghz, 4 ghz, and 6 ghz frequency bands," in *2016 IEEE 83rd Vehicular Technology Conference (VTC Spring)*, 2016, pp. 1–5.

[13] M. Lei, J. Zhang, T. Lei, and D. Du, "28-ghz indoor channel measurements and analysis of propagation characteristics," in *2014 IEEE 25th Annual International Symposium on Personal, Indoor, and Mobile Radio Communication (PIMRC)*, 2014, pp. 208–212.

[14] M. Samimi, K. Wang, Y. Azar, G. N. Wong, R. Mayzus, H. Zhao, J. K. Schulz, S. Sun, F. Gutierrez, and T. S. Rappaport, "28 ghz angle of arrival and angle of departure analysis for outdoor cellular communications using steerable beam antennas in new york city," in *2013 IEEE 77th Vehicular Technology Conference (VTC Spring)*, 2013, pp. 1–6.

[15] H. Schwan, "Interaction of microwave and radio frequency radiation with biological systems," *IEEE Transactions on Microwave Theory and Techniques*, vol. 19, no. 2, pp. 146–152, 1971.

[16] M. Bonato, L. Dossi, E. Chiaramello, S. Fiocchi, S. Gallucci, G. Tognola, P. Ravazzani, and M. Parazzini, "Single user emf exposure assessment in a case of incoming 5g indoor scenario," in *2020 International Symposium on Electromagnetic Compatibility - EMC EUROPE*, 2020, pp. 1–4.

[17] S. Gallucci, M. Bonato, M. Benini, E. Chiaramello, S. Fiocchi, G. Tognola, and M. Parazzini, "Human rf-emf exposure assessment for a wearable device by stochastic dosimetry," in *2022 Microwave Mediterranean Symposium (MMS)*, 2022, pp. 1–4.

[18] M. Bonato, L. Dossi, E. Chiaramello, S. Fiocchi, S. Gallucci, G. Tognola, P. Ravazzani, and M. Parazzini, "Human rf-emf exposure assessment due to access point in incoming 5g indoor scenario," *IEEE Journal of Electromagnetics, RF and Microwaves in Medicine and Biology*, vol. 5, no. 3, pp. 269–276, 2021.

[19] D. Colombi, B. Thors, C. TöRnevik, and Q. Balzano, "Rf energy absorption by biological tissues in close proximity to millimeter-wave 5g wireless equipment," *IEEE Access*, vol. 6, pp. 4974–4981, 2018.

[20] L. Huclová, D. Erni, and J. Fröhlich, "Modelling and validation of dielectric properties of human skin in the mhz region focusing on skin layer morphology and material composition," *Journal of Physics D: Applied Physics*, vol. 45, no. 2, p. 025301, 2012.

[21] N. B. M. Tamyis, D. K. Ghodgaonkar, M. N. Taib, and W. T. Wui, "Dielectric properties of human skin *in vivo* in the frequency range of 20–38 ghz for 42 healthy volunteers," in *Proceedings of the URSI General Assembly*. New Delhi, India: International Union of Radio Science (URSI), 2005, p. KP.45–KP.50.

[22] M. S. Alghamdi and N. A. El-Ghazaly, "Effects of exposure to electromagnetic field on some hematological parameters in mice," *Open Journal of Medicinal Chemistry*, vol. 2, no. 2, pp. Article ID 19 684, 13 pages, 2012, received March 1, 2012; revised April 5, 2012; accepted April 14, 2012.

[23] A. La Gioia, E. Porter, I. Merunka, A. Shahzad, S. Salahuddin, M. Jones, and M. O'Halloran, "Open-ended coaxial probe technique for dielectric measurement of biological tissues: Challenges and common practices," *Diagnostics*, vol. 8, no. 2, 2018. [Online]. Available: https://www.mdpi.com/2075-4418/8/2/40

[24] A. Kraszewski, M. A. Stuchly, and S. S. Stuchly, "Ana calibration method for measurements of dielectric properties," *IEEE Transactions on Instrumentation and Measurement*, vol. 32, no. 2, pp. 385–387, 1983.

[25] I. Dilman, M. N. Akinci, T. Yilmaz, M. Çayören, and I. Akduman, "A method to measure complex dielectric permittivity with open-ended coaxial probes," *IEEE Transactions on Instrumentation and Measurement*, vol. 71, pp. 1–7, 2022.

[26] K.-F. Lee and K.-F. Tong, "Microstrip patch antennas—basic characteristics and some recent advances," *Proceedings of the IEEE*, vol. 100, no. 7, pp. 2169–2180, 2012.

[27] TMYTEK and National Instruments, "Bbox one datasheet (5g 28 ghz)," December 2022, accessed: 2025-07-31. [Online]. Available: https://docs-be.ni.com/bundle/tmytek-ni-bbox-one-datasheet/raw/resource/enus/tmytek-ni-bbox-one-datasheet.pdf

[28] T. K. Geok, F. Hossain, M. N. Kamaruddin, N. Z. A. Rahman, S. Thiagarajah, A. T. W. Chiat, J. Hossen, and C. P. Liew, "A comprehensive review of efficient ray-tracing techniques for wireless communication," *International Journal*

on Communications Antenna and Propagation (I.Re.C.A.P.), vol. 8, no. 2, pp. 123–??, 2018.

[29] Altair Engineering Inc., *Altair WinProp User Guide*, https://help.altair.com/winprop/pdf/Altair_WinProp_User_Guide.pdf, Altair Engineering Inc., 2025, updated May 22, 2025.

[30] S. S. Kalamkar, F. Baccelli, F. M. Abinader, A. S. M. Fani, and L. G. U. Garcia, "Beam management in 5g: A stochastic geometry analysis," *IEEE Transactions on Wireless Communications*, vol. 21, no. 4, pp. 2275–2290, 2022.

[31] M. D. Migliore and F. Schettino, "Power reduction estimation of 5g active antenna systems for human exposure assessment in realistic scenarios," *IEEE Access*, vol. 8, pp. 220 095–220 107, 2020.

[32] IFAC-CNR, "Tissue properties database," http://niremf.ifac.cnr.it/tissprop/htmlclie/htmlclie.php, 2025, accessed: 2025-08-19.

[33] K. Sasaki, K. Wake, and S. Watanabe, "Measurement of the dielectric properties of the epidermis and dermis at frequencies from 0.5 ghz to 110 ghz," *Physics in Medicine & Biology*, vol. 59, no. 16, pp. 4739–4747, 2014.

[34] J. Malmivuo and R. Plonsey, *Bioelectromagnetism: Principles and Applications of Bioelectric and Biomagnetic Fields*. New York: Oxford University Press, 1995, accessed: 2025-08-19. [Online]. Available: http://www.bem.fi/book

[35] I. D. Lubangakene, B. Virdee, R. K. R. Jayanthi, and P. Ganguly, "Effect of metabolite and temperature on artificial human sweat characteristics over a very wide frequency range (400 mhz–10.4 ghz) for wireless hydration diagnostic sensors," *Results in Engineering*, vol. 19, p. 101328, 2023. [Online]. Available: https://www.sciencedirect.com/science/article/pii/S2590123023004553

[36] A. Ponomarenko, V. Artyukhov, N. Nechaeva, Y. Uspenskaya, Y. Bozhevolnov, S. Gudkov, B. Shub, S. Tishkin, V. Tkachenko, R. Sharipov, E. Kistenev, A. Nikitin, A. Ponomarenko, and A. Mamedov, "The effect of a high frequency electromagnetic field in the microwave range on red blood cells," *Scientific Reports*, vol. 7, no. 1, p. 10752, 2017. [Online]. Available: https://www.nature.com/articles/s41598-017-11288-9

[37] M. Shmukler, *Density of Blood*. The Physics Factbook, 2004, average density of whole human blood 1060 kg/m^3. [Online]. Available: https://hypertextbook.com/facts/2004/MichaelShmukler.shtml

Appendix

Index	1	2	3	4	5	6	7	8	9	10	11	12	13	14
Azimuth °	107	90	73	141	127	104	76	53	39	162	158	150	136	109
Elevation °	12	13	12	25	31	36	36	31	25	28	33	41	50	59

15	16	17	18	19	20	21	22	23	24	25	26	27	28	29
71	71	44	30	22	18	178	177	176	159	21	7	4	3	2
59	50	41	33	28	29	35	45	59	78	78	59	45	35	29

Table 4.1: Rotation angles of grid of beams

Database	Addition transmitted power [dBm]
Presentation	13.4381, 13.0905, 13.44, 7.3665, 5.8493, 4.69970, 4.6857, 5.8497, 7.3671, 6.4823, 5.1381, 3.683, 2.3074, 1.3953, 1.3945, 2.3062, 3.6828, 5.138, 7.4098, 4.7386,3.4684, 2.0703, 1.0472,0.274, 0, 1.0515,2.0736, 3.4717, 4.7419,
Meeting	12.7176, 12.8221, 13.06, 7.0925, 5.4129, 4.4142, 4.2827, 5.5193, 7.0931, 6.2086, 4.8639, 3.409, 2.0334, 1.1213, 1.1213, 2.0334, 3.4088, 4.8639, 7.1358, 4.4646, 3.1944, 1.7963, 0.7732, 0, 0.0032, 0.7767, 1.7997, 3.1977, 4.4679

Table 4.2: Additional transmitted power of scenarios

Figure 4.1: Measurement setup of BBox broadside pattern in the Dome

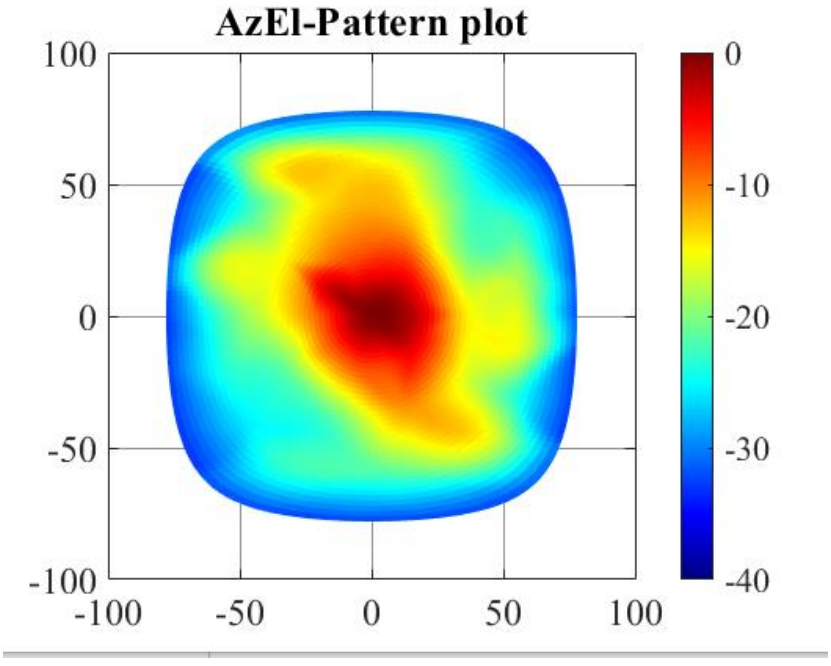

Figure 4.2: BBox broadside pattern of the Dome measurement